Computers and Fluids 124 (2016) 278–287

Contents lists available at ScienceDirect

Computers and Fluids

journal homepage: www.elsevier.com/locate/compfluid

Anisotropic thermal lattice Boltzmann simulation of 2D natural convection in a square cavity

François Dubois [a,b], Chao-An Lin [c], Mohamed Mahdi Tekitek [c,d,*]

[a] Department of Mathematics, Paris-Sud University, Orsay, France
[b] Conservatoire National des Arts et Métiers, LMSSC, Paris, France
[c] Department of Power Mechanical Engineering, National Tsing Hua University, Hsinchu 30013, Taiwan
[d] Department of Mathematics, Faculty of Sciences of Tunis, University of Tunis El Manar, 2092 El Manar, Tunisia

ARTICLE INFO

Article history:
Received 9 January 2015
Revised 15 October 2015
Accepted 22 October 2015
Available online 6 November 2015

Keywords:
Thermal lattice Boltzmann model
Multiple relaxation time model
Double population
Natural convection
Square cavity

ABSTRACT

Natural convection in a square cavity is simulated by multiple relaxation time (MRT) lattice Boltzmann method (LBM) with a separate distribution function to solve for the temperature distribution. The Rayleigh numbers examined range from $Ra = 10^3$ to $Ra = 10^6$. The simulations are performed for anisotropic thermal case and compared to isotropic thermal case.

1. Introduction

Lattice Boltzmann method (LBM) [2,26,37,39] has been successfully applied to various hydrodynamic problems and the major advantage of the LBM is explicit formulation. However, its application to non-isothermal problem is limited because of the numerical instability for thermal models [32]. In general, there are three thermal lattice Boltzmann methods (TLBM) named the multi speed approach [1], the passive scalar approach and the double population approach.

The multi-speed approach adopts a single distribution function in order to obtain the macroscopic dynamic and thermal equations [1]. However, the Prandtl number is fixed and this approach suffers from lack of numerical stabilities.

The passive scalar approach also called hybrid method, consists of solving velocity field using LBM and the macroscopic temperature is solved by different numerical methods (e.g. finite difference or finite volume) [24,30]. This approach is more stable than the multi speed approach. But it has two disadvantages: first the viscous heat dissipation and compression work done by pressure cannot be incorporated, and second the simplicity of LBM is lost.

The double population method, is first used by He et al. [19]. This approach can be regarded as another version of the passive scalar method. In fact to solve macroscopic temperature another LBM distribution is used. This model has a better numerical stability than the multi speed approach, and the viscous heat dissipation and compression work done by the pressure can be solved implicitly. Peng et al. [35] proposed a simplified thermal energy distribution model where the compression work done by the pressure and the viscous heat dissipation are neglected. By introducing a forcing function, Guo et al. [17] proposed a thermal lattice BGK equation with viscous heat dissipation in the incompressible limit.

The thermally driven cavity with adiabatic top and bottom walls (also called natural convection in a square cavity) is a classical benchmark to examine the accuracy of the scheme. The solution is given for 4 values of the Rayleigh number (Ra), ($Ra = 10^3, 10^4, 10^5$ and 10^6). The value of the Prandtl number (Pr) is equal to 0.71, which corresponds to a cavity filled by air. The reference solution of this problem is given by De Vahl Davis [4].

To validate double population LBM method few researchers [10,16,18,21,29] have carried out the above problem. We note here that most of this works are using simple relaxation time (SRT), also called Lattice Boltzmann Bhatngar–Gross–Krook (LBGK). This is due to extreme simplicity of this method. Even that LBGK suffers from lack of numerical stability and inaccuracy in implementing boundary conditions.

* Corresponding author at: Department of Mathematics, Faculty of Sciences of Tunis, University of Tunis El Manar, 2092 El Manar, Tunisia. Tel: +216 98901903.
E-mail address: mahdi.tekitek@math.u-psud.fr, memotek@gmail.com (M.M. Tekitek).

http://dx.doi.org/10.1016/j.compfluid.2015.10.015
0045-7930/

In this paper we present a double population approach using multiple relaxation time lattice Boltzmann method (MRT-LBM) [38] with D2Q9 lattice model for solving velocity field and another D2Q9 for solving macroscopic temperature. The choice of D2Q9 model for thermal is to be able to model anisotropic thermal diffusion. We note that anisotropic thermal diffusion have many applications in diffusivity study of gas diffusion layer (see [34] for measurements and [11] for computations), advection and anisotropic-dispersion equation, porous media (see *e. g.* [7,13,15]).

First we consider natural convection in a square cavity when the flow is laminar (i.e. Rayleigh number is less than 10^6.). To validate our model, we choose isotropic thermal diffusivity (i.e. diffusivity in x direction κ_x is equal to diffusivity in y direction κ_y). Then we consider anisotropic thermal diffusion. In fact we consider two cases $\kappa_x = \kappa_y/2$ and $\kappa_x = 2\kappa_y$, and we compare the solution to the isotropic one.

This paper is organized as follows. In Section 2, a brief overview of the MRT D2Q9 for advection-diffusion and the MRT D2Q9 for fluid problem. After in Section 3 we introduce the thermal LBM for the simulation of a Boussinesq fluid in a square cavity. In Section 4, results are presented and discussed. Finally, in Section 5 we conclude.

2. Multi relaxation time lattice Boltzmann method

2.1. Dynamic field

The multi relaxation time (MRT) lattice Boltzmann method [23] can be expressed as:

$$m_l^*(\vec{x},t) = m_l(\vec{x},t) - S_{lj}[m_j(\vec{x},t) - m_j^{eq}(\vec{x},t)] \tag{1}$$

$$f_i(\vec{x}+\vec{e}_i\triangle t, t+\triangle t) = M_{il}^{-1} m_l^*(\vec{x},t) \tag{2}$$

m_l^*, Eq. (1), is the collision at the moment space and Eq. (2) represents the streaming operation. Here, $\mathbf{M}$ is a matrix that transforms the distribution function $\mathbf{f}$ to the velocity moment, $\mathbf{m}$=$\mathbf{Mf}$, and $\mathbf{S}$ is the relaxation matrix. These will be defined later.

Based on the particle distribution functions, the macroscopic density and velocity are defined as:

$$\sum_i f_i = \rho, \quad \sum_i f_i \vec{e}_i = \rho \vec{u}. \tag{3}$$

For the present 2D applications, D2Q9 model are adopted to model fluid problems and the particle speed $\vec{e}_i$ are defined as,

$$\begin{cases} \vec{e}_0 = 0, \\ \vec{e}_i = (\cos[\pi(i-1)/2], \sin[\pi(i-1)/2])c, \\ \quad \text{for } i = 1,2,3,4, \\ \vec{e}_i = (\cos[\pi(i-4-1/2)/2], \sin[\pi(i-4-1/2)/2])\sqrt{2}c, \\ \quad \text{for } i = 5,6,7,8, \end{cases}$$

where $c = dx/dt$ is the lattice speed, and dx and dt are the lattice width and time step, respectively. Here, dt is chosen to be equal to dx, thus $c = 1$. Moreover, the speed of sound is $C_s = c/\sqrt{3}$.

The transformation matrix $\mathbf{M}$ and the velocity moment vector $\mathbf{m}$ are defined as,

$$\underbrace{\begin{bmatrix} m_0\ (\rho) \\ m_1\ (e) \\ m_2\ (\varepsilon) \\ m_3\ (j_x) \\ m_4\ (q_x) \\ m_5\ (j_y) \\ m_6\ (q_y) \\ m_7\ (p_{xx}) \\ m_8\ (p_{xy}) \end{bmatrix}}_{\mathbf{m}} = \underbrace{\begin{bmatrix} 1 & 1 & 1 & 1 & 1 & 1 & 1 & 1 & 1 \\ -4 & -1 & -1 & -1 & -1 & 2 & 2 & 2 & 2 \\ 4 & -2 & -2 & -2 & -2 & 1 & 1 & 1 & 1 \\ 0 & 1 & 0 & -1 & 0 & 1 & -1 & -1 & 1 \\ 0 & -2 & 0 & 2 & 0 & 1 & -1 & -1 & 1 \\ 0 & 0 & 1 & 0 & -1 & 1 & 1 & -1 & -1 \\ 0 & 0 & -2 & 0 & 2 & 1 & 1 & -1 & -1 \\ 0 & 1 & -1 & 1 & -1 & 0 & 0 & 0 & 0 \\ 0 & 0 & 0 & 0 & 0 & 1 & -1 & 1 & -1 \end{bmatrix}}_{\mathbf{M}} \underbrace{\begin{bmatrix} f_0 \\ f_1 \\ f_2 \\ f_3 \\ f_4 \\ f_5 \\ f_6 \\ f_7 \\ f_8 \end{bmatrix}}_{\mathbf{f}} \tag{4}$$

and the equilibria of the velocity moments $\mathbf{m}^{eq}$ are,

$$\begin{cases} \rho^{eq} = \rho, \quad e^{eq} = -2\rho + \frac{3}{\rho}(j_x^2 + j_y^2), \quad \epsilon^{eq} = \rho - \frac{3}{\rho}(j_x^2 + j_y^2), \\ j_x^{eq} = j_x, \quad q_x^{eq} = -j_x, \quad j_y^{eq} = j_y, q_y^{eq} = -j_y, \\ p_{xx}^{eq} = \frac{1}{\rho}(j_x^2 - j_y^2), \quad p_{xy}^{eq} = \frac{j_x j_y}{\rho}. \end{cases} \tag{5}$$

The relaxation matrix $\mathbf{S}$ is a diagonal matrix, i.e.,

$$\mathbf{S} = diag[s_0, s_1, s_2, s_3, s_4, s_5, s_6, s_7, s_8] \tag{6}$$

where $s_0 = s_3 = s_5 = 0$ enforces mass and momentum conservation before and after collision [23]. Here, $s_4 = s_6 \equiv s_q$, $s_7 = s_8 \equiv s_\nu$, thus the viscosity formulation is the same as that by the SRT model as shown in [23], *i.e.* the corresponding kinematic viscosity is $\nu = (\frac{1}{s_\nu} - \frac{1}{2})C_s^2 dt$ in the simulation. More specifically, we choose to use the following relationship between two relaxation rates: $s_q = 8\frac{(2-s_\nu)}{(8-s_\nu)}$ where $s_q \equiv s_4 = s_6$. See [8,14] for more details.

We note that, the MRT model can recover to SRT model if $s_1 = s_2 = s_4 = s_6 = s_7 = s_8 = s_\nu$.

2.2. Thermal field

The thermal field is modeled using the passive scalar approach to enhance the numerical stability, where a separate distribution function is used to solve for the temperature distribution [27,35,36]. The D2Q9 model introduced in the above section is adopted. The evolution of the scalar MRT LB scheme is given as:

$$\widetilde{m}_l^*(\vec{x},t) = \widetilde{m}_l(\vec{x},t) - \sigma_{lj}[\widetilde{m}_j(\vec{x},t) - \widetilde{m}_j^{eq}(\vec{x},t)] \tag{7}$$

$$g_i(\vec{x}+\vec{e}_i\triangle t, t+\triangle t) = M_{il}^{-1}\widetilde{m}_l^*(\vec{x},t) \tag{8}$$

Here, f_i is replaced by g_i in Eq. (2), because g_i is now the energy distribution function. The transformation matrix is the same as in equation (4), thus $\widetilde{\boldsymbol{m}} = \mathbf{Mg}$. Again, $\widetilde{m}_l^*$ is the scalar collision at the moment space. $\boldsymbol{\sigma}$ is the diagonal relaxation matrix, *i.e.*

$$\boldsymbol{\sigma} = diag[\sigma_0, \sigma_1, \sigma_2, \sigma_3, \sigma_4, \sigma_5, \sigma_6, \sigma_7, \sigma_8] \tag{9}$$

where $\sigma_0 = 0$ enforces energy conservation, $\widetilde{m}_0 = \sum_i g_i = T$, before and after collision.

The equilibrium values $\widetilde{m}_i^{eq}$ of the nonconserved moments are given by (see [22] for more details) :

$$\begin{aligned} \widetilde{m}_1^{eq} &= \widetilde{\alpha}T + 3T(u^2+v^2), \\ \widetilde{m}_2^{eq} &= \widetilde{\beta}T, \\ \widetilde{m}_3^{eq} &= uT, \\ \widetilde{m}_4^{eq} &= uT(-1+3(u^2+v^2)), \\ \widetilde{m}_5^{eq} &= vT, \\ \widetilde{m}_6^{eq} &= vT(-1+3(u^2+v^2)) \\ \widetilde{m}_7^{eq} &= a_xT + T(u^2-v^2), \\ \widetilde{m}_8^{eq} &= a_yT + T(uv), \end{aligned}$$

where $\mathbf{V} \equiv (u, v)$ is the dynamic field.

Using Taylor expansion [5,6] or Chapman–Enskog procedure [12], the advection diffusion [15] equation with an-isotropic coefficient up to order two in Δt can be expressed as:

$$\begin{aligned} \frac{\partial T}{\partial t} + U\frac{\partial T}{\partial t} + V\frac{\partial T}{\partial y} = &\frac{C_s^2 dt}{2}\left(\frac{1}{2} - \frac{1}{\sigma_3}\right)(\widetilde{\alpha} + 3a_x + 4)\frac{\partial^2 T}{\partial x^2} \\ &+ \frac{C_s^2 dt}{2}\left(\frac{1}{2} - \frac{1}{\sigma_5}\right)(\widetilde{\alpha} + 3a_x + 4)\frac{\partial^2 T}{\partial y^2} \\ &+ \frac{3C_s^2 dt}{2}a_y\left(\frac{1}{\sigma_3} + \frac{1}{\sigma_5} - 1\right)\frac{\partial^2 T}{\partial xy}, \end{aligned}$$

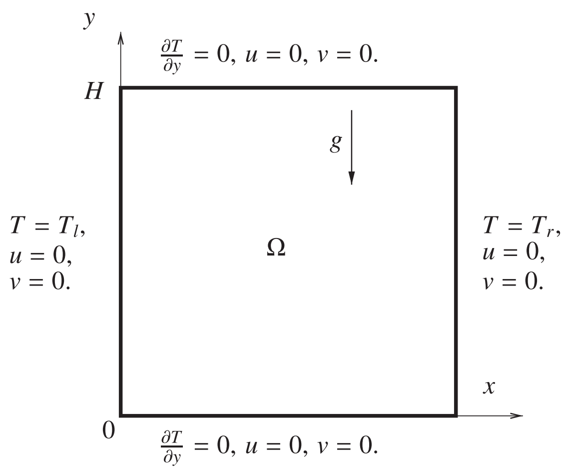

Fig. 1. Configuration of natural convection in a square cavity.

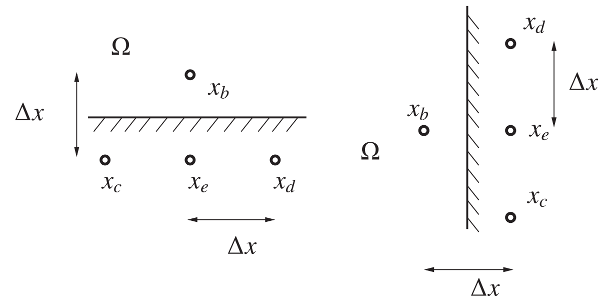

Fig. 2. Left: Boundary node x_b in the bottom of the domain Ω. Right: Boundary node x_b in the right of the domain Ω.

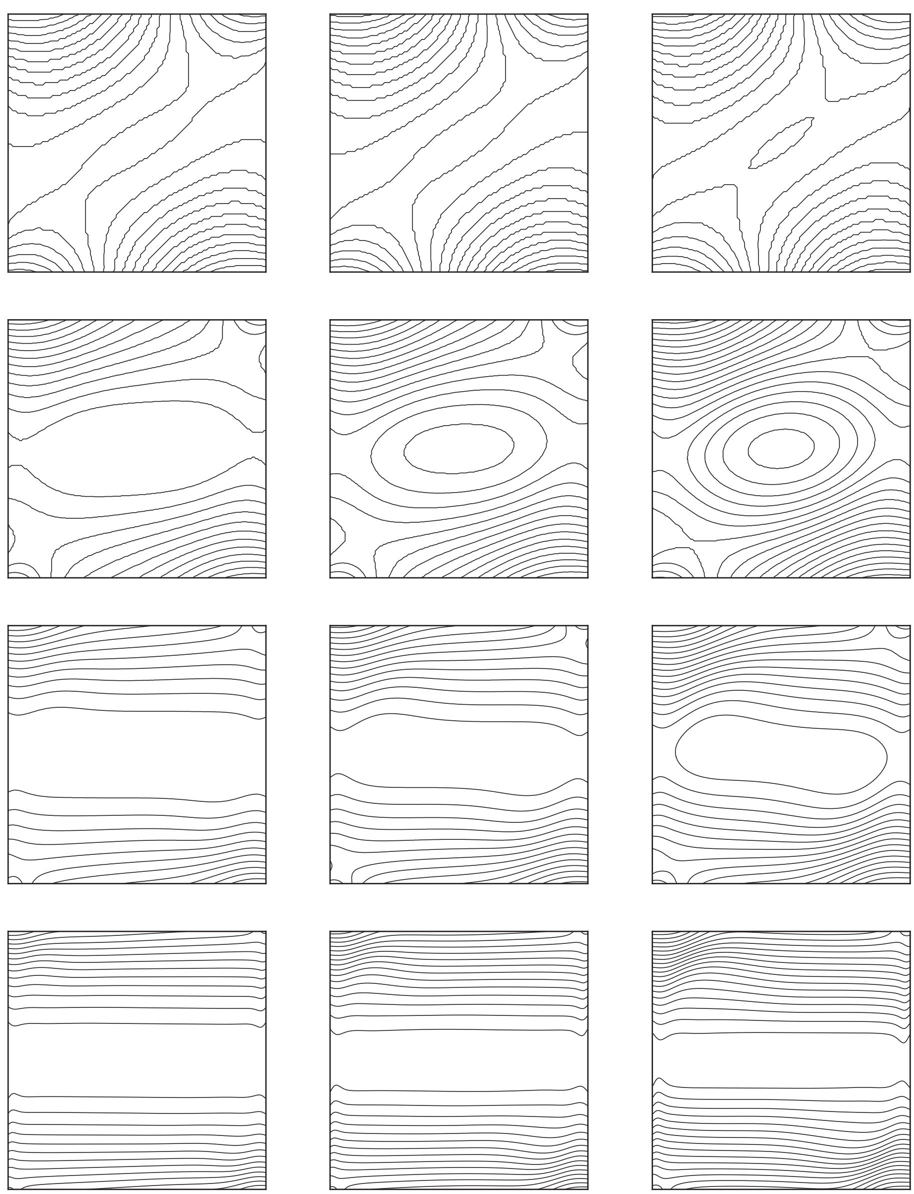

Fig. 3. Isobars (P) of flow fields for Pr=0.71. From top to bottom $Ra = 10^3$, 10^4, 10^5, and 10^6 respectively for mesh size 105^2, 155^2, 205^2 and 255^2. From left to right : (left) $\kappa_x = \kappa_y/2$, (center) isotropic case $\kappa_x = \kappa_y$,(right) $\kappa_x = 2\kappa_y$.

Table 1
Grid dependence and order of accuracy for numerical results of simulating 2-D natural convection of air in a square cavity for the case $Ra = 10^6$.

Mesh size	$\overline{Nu}$	u_{max}	y	v_{max}	x
47^2	9.5729	64.6766	0.8414	222.8704	$3.6585.10^{-2}$
57^2	9.2079	64.8453	0.8508	218.5256	$4.3859.10^{-2}$
81^2	8.8913	64.8181	0.8456	218.6303	$4.3209.10^{-2}$
161^2	8.7828	64.8375	0.8478	220.1784	$4.0372.10^{-2}$
225^2	8.8006	64.8393	0.8511	220.7288	$3.7777.10^{-2}$
321^2	8.8139	64.8403	0.8489	220.5115	$3.8940.10^{-2}$
615^2	8.8226	64.8391	0.8495	220.5741	$3.8211.10^{-2}$
Reference solution	8.8241	64.8372	0.8495	220.5739	$3.7993.10^{-2}$
Accuracy	2.109	2.0154	1.9261	2.0592	1.7571
Davis [4]	8.817	64.630	0.850	219.360	$3.8.10^{-2}$
Le Quéré [25]	8.825	64.483	0.850	220.559	$3.8.10^{-2}$

Table 2
Grid dependence and order of accuracy for numerical results of simulating 2-D natural convection of air in a square cavity for the case $Ra = 10^8$.

Mesh size	Nu	U_{max}	Y	V_{max}	X
495^2	29.97	313.97	0.926	2219.3	0.011
987^2	30.20	319.81	0.927	2222.8	0.011
2016^2	30.22	321.59	0.928	2222.7	0.012
Le Quéré [25]	30.22	321.88	0.928	2222.2	0.012

Table 3
Comparison of predicted numerical results. Davis [4], Mayne et al. [31], Liu et al. [28], Dixit et al. [10], Kuznik et al. [21], Mezrhab et al. [33] and Wang et al. [38].

Ra		[4]	[31]	[28]	[21]	[33]	[38]	**Present**
10^3	u_{max}	3.649	3.649	3.649	3.636	3.667	3.649	3.649
	y	0.813	0.812	0.810	0.809	–	0.813	0.814
	v_{max}	3.697	3.696	3.698	3.686	3.714	3.697	3.697
	x	0.178	0.179	0.180	0.174	–	0.178	0.176
	$\overline{Nu}$	1.117	1.114	1.115	1.117	1.112	1.117	1.117
10^4	u_{max}	16.178	16.179	16.154	16.167	16.202	16.183	16.188
	y	0.823	0.823	0.820	0.821	–	0.823	0.822
	v_{max}	19.617	19.617	19.614	19.597	19.644	19.627	19.632
	x	0.119	0.119	0.120	0.120	–	0.118	0.119
	$\overline{Nu}$	2.243	2.259	2.229	2.246	2.241	2.244	2.243
10^5	u_{max}	34.730	34.774	34.508	34.962	34.805	34.743	34.748
	y	0.855	0.853	0.855	0.854	–	0.854	0.856
	v_{max}	68.590	68.692	68.595	68.578	68.630	68.631	68.652
	x	0.066	0.066	0.065	0.067	–	0.065	0.065
	$\overline{Nu}$	4.519	4.483	4.489	4.518	4.519	4.521	4.517
10^6	u_{max}	64.630	64.691	63.456	64.133	64.793	64.827	64.842
	y	0.850	0.846	0.848	0.860	–	0.849	0.849
	v_{max}	219.360	220.833	219.788	220.537	219.663	220.550	220.669
	x	0.037	0.038	0.036	0.038	–	0.037	0.037
	$\overline{Nu}$	8.799	8.881	8.750	8.792	8.817	8.819	8.806

Table 4
Convergence for the case $Ra_y = 10^6$ and $\kappa_x = \frac{\kappa_y}{2}$.

Mesh size	$\overline{Nu}$	u_{max}	y	v_{max}	x
47^2	23.1332	50.5699	0.8919	168.2357	$3.2749.10^{-2}$
57^2	22.2512	50.7018	0.9019	164.9560	$3.9260.10^{-2}$
81^2	21.4861	50.6805	0.8963	165.0350	$4.3209.10^{-2}$
161^2	21.2239	50.6957	0.8987	166.2036	$3.6139.10^{-2}$
225^2	21.2805	50.6999	0.9000	166.5744	$3.3333.10^{-2}$
321^2	21.2991	50.6979	0.8998	166.4551	$3.4857.10^{-2}$
615^2	21.3201	50.6970	0.9005	166.5023	$3.4205.10^{-2}$
Reference solution	21.3237	50.6955	0.9005	166.5022	$3.4009.10^{-2}$
Accuracy	2.1009	2.0582	1.9368	2.0855	1.7009

Table 5
Convergence for the case $Ra_y = 10^6$ and $\kappa_x = 2\kappa_y$.

Mesh size	$\overline{Nu}$	u_{max}	y	v_{max}	x
47^2	3.8261	119.7447	0.8569	285.6379	$4.0420.10^{-2}$
57^2	3.6802	120.0571	0.8665	280.0695	$4.8457.10^{-2}$
81^2	3.5537	120.0067	0.8612	280.2036	$4.7738.10^{-2}$
161^2	3.5103	120.0426	0.8634	282.1877	$4.4604.10^{-2}$
225^2	3.5174	120.0460	0. 8668	282.8932	$4.1737.10^{-2}$
321^2	3.5227	120.0478	0.8645	282.6147	$4.3022.10^{-2}$
615^2	3.5262	120.0456	0.8652	282.6949	$4.2216.10^{-2}$
Reference solution	3.5268	120.0421	0.8652	282.6946	$4.1976.10^{-2}$
Accuracy	2.1747	2.0581	1.8891	2.3270	1.7507

Table 6
Predicted numerical results for different cases: $\kappa_x = \frac{\kappa_y}{2}$, $\kappa_x = \kappa_y$ and for $\kappa_x = 2\kappa_y$.

Ra		$\kappa_x = \frac{\kappa_y}{2}$	$\kappa_x = \kappa_y$	$\kappa_x = 2\kappa_y$
10^3	u_{max}	3.3705	3.6496	3.8185
	y	0.8142	0.8142	0.8142
	v_{max}	3.4515	3.6973	3.8428
	x	0.1761	0.1761	0.1857
	$\overline{Nu}$	2.4957	1.1179	0.5226
10^4	u_{max}	12.3628	16.1881	21.1512
	y	0.8290	0.8225	0.8225
	v_{max}	16.0159	19.6323	24.0035
	x	0.1064	0.1193	0.1322
	$\overline{Nu}$	5.3711	2.2438	0.9261
10^5	u_{max}	23.5783	34.7486	56.0032
	y	0.8560	0.8560	0.8609
	v_{max}	53.5863	68.6527	86.0559
	x	0.0609	0.0658	0.0707
	$\overline{Nu}$	10.9325	4.5177	1.8262
10^6	u_{max}	50.6999	64.8428	120.0525
	y	0.9000	0.8490	0.8647
	v_{max}	166.5744	220.6695	282.8172
	x	0.0333	0.0372	0.0411
	$\overline{Nu}$	21.2805	8.8062	3.5197

Let $a_x = a_y = 0$, the above advection diffusion equation is reduced to equation anisotropic diffusion coefficient and is expressed as:

$$\frac{\partial T}{\partial t} + \mathbf{V}.\nabla T = \kappa_x \frac{\partial^2 T}{\partial x^2} + \kappa_y \frac{\partial^2 T}{\partial^2 y}, \tag{10}$$

where the values of x-diffusivity κ_x and y-diffusivity κ_y are :

$$\kappa_x = C_s^2 dt \frac{\widetilde{\alpha}+4}{2}\left(\frac{1}{\sigma_3} - \frac{1}{2}\right), \quad \kappa_y = C_s^2 dt \frac{\widetilde{\alpha}+4}{2}\left(\frac{1}{\sigma_5} - \frac{1}{2}\right). \tag{11}$$

Here, $\widetilde{\alpha}$ and $\widetilde{\beta}$ are -2 and 1, respectively. The present D2Q9 advection diffusion equation can accommodate thermal problem with isotropic (*i. e.* $\kappa_x = \kappa_y = \kappa$) diffusivity [7]. When $U = V = 0$, Eq. (10) reduces to diffusion equation.

Remark Note here that using D2Q5 for thermal problem (see [3]) and isotropic diffusivity is sufficient, faster and requires less memory than using D2Q9. The advantages of using Thermal D2Q9 is the ability to model non isotropic thermal problem and the possibility to cancel the dependence of thermal diffusivity on the advection velocity (for more details see [22]).

2.3. Coupling of dynamic and thermal fields

With the Boussinesq approximation, the buoyancy term is assumed to depend linearly on the temperature as,

$$F_y = \beta g_y (T - T_{ref}) \tag{12}$$

where β is the thermal expansion coefficient, g_y is the acceleration due to gravity, and T_{ref} is the reference temperature.

To perform the coupling, the buoyancy force F_y is added in moment space before and after the collision process of the LB scheme as described by Eq. (1). The procedure goes like this [9]:

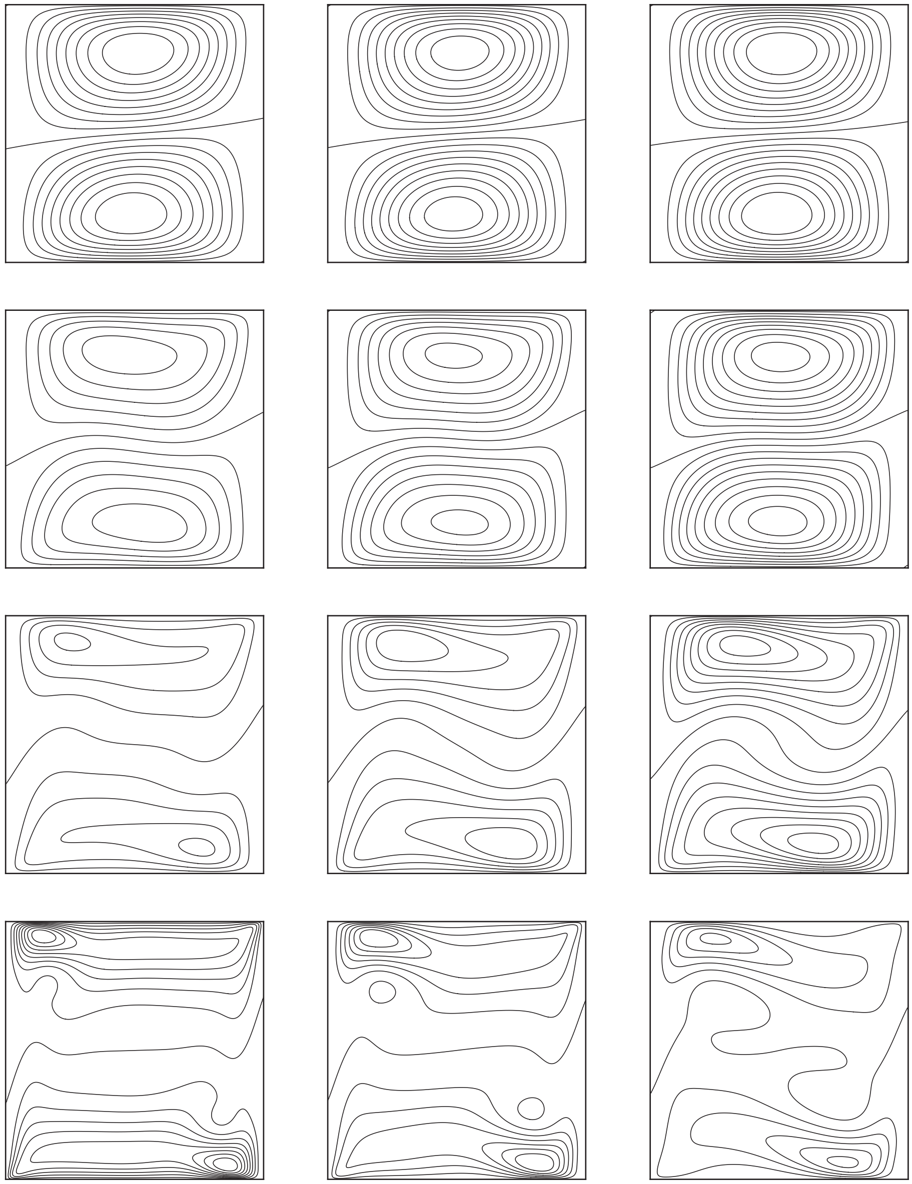

Fig. 4. First component of velocity (U) of flow for Pr=0.71. From top to bottom $Ra = 10^3$, 10^4, 10^5, and 10^6 respectively for mesh size 105^2, 155^2, 205^2 and 255^2. From left to right : (left) $\kappa_x = \kappa_y/2$, (center) isotropic case $\kappa_x = \kappa_y$,(right) $\kappa_x = 2\kappa_y$.

- The y direction momentum (j_y) and energy flux (q_y) are modified by adding half of the external force F_y, i.e.

$$\bar{j}_y = j_y + \frac{\Delta t}{2}F_y, \quad \bar{q}_y = q_y - \frac{\Delta t}{2}F_y,$$

- Compute the equilibrium moments in Eq. (5) using $\bar{j}_y$ and $\bar{q}_y$ to replace j_y and q_y.
- Perform collision in Eq. (1).
- Post collision y direction momentum and energy flux are modified by adding another half of the external force, i.e.,

$$\bar{j}^*_y = j^*_y + \frac{\Delta t}{2}F_y, \quad \bar{q}^*_y = q^*_y - \frac{\Delta t}{2}F_y,$$

- Perform streaming in Eq. (2) using $\bar{j}^*_y$ and $\bar{q}^*_y$ to replace j^*_y and q^*_y.

Other forms of forcing term accounted for the discrete effect could also be adopted [17]. It is noted that the compressibility may influence the results, and this can be eliminated by incompressible model [20]. However, since the present Mach number is low, therefore this influence could be neglected [35].

2.4. Geometry and boundary conditions

Natural convection in a square cavity $\Omega =]0, H[\times]0, H[$ (see Fig. 1) is considered, where the flow is bounded by a stationary square enclosure with sidewalls maintained at different temperatures and driven by the buoyancy force. For laminar convection in this flow configuration, the viscous heat dissipation is assumed to be negligible. The temperature difference between the walls introduces a temperature gradient in the fluid, and the consequent density difference induces a convective fluid motion. The left wall is at the higher uniform temperature T_l and the right wall is at the lower uniform temperature T_r. Both the top and bottom walls are adiabatic, i.e. $\partial T/\partial y = 0$. The summary of the boundary conditions is shown below.

$$u = v = 0 \text{ on } \partial\Omega \tag{13}$$

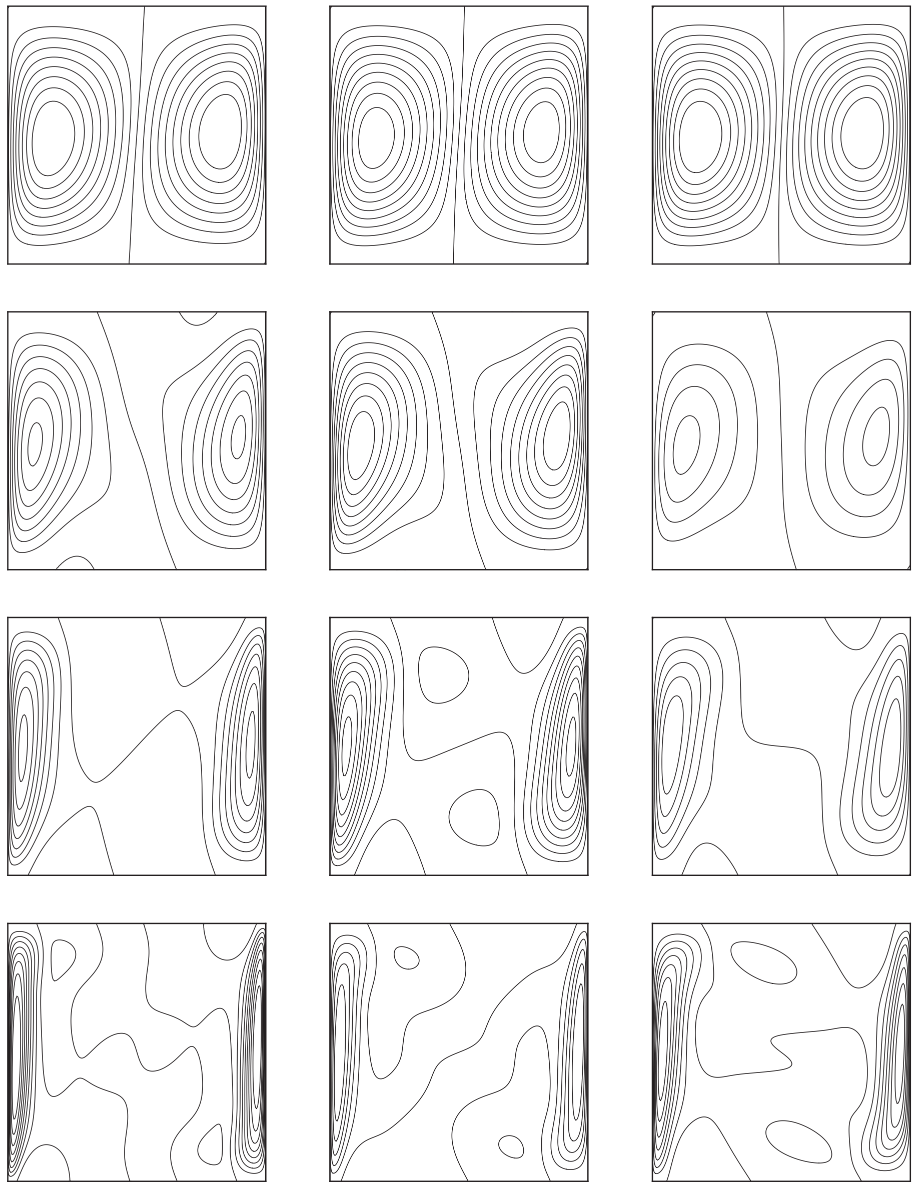

Fig. 5. Second component of velocity (V) of flow for Pr=0.71. From top to bottom $Ra = 10^3$, 10^4, 10^5, and 10^6 respectively for mesh size 105^2, 155^2, 205^2 and 255^2. From left to right: (left) $\kappa_x = \kappa_y/2$, (center) isotropic case $\kappa_x = \kappa_y$, (right) $\kappa_x = 2\kappa_y$.

$$T = T_l \text{ on } \{0\} \times [0, H] \tag{14}$$

$$T = T_r \text{ on } \{H\} \times [0, H] \tag{15}$$

$$\frac{\partial T}{\partial y} = 0 \text{ on } [0, H] \times \{0\} \text{ and } [0, H] \times \{H\} \tag{16}$$

For Dirichlet boundary condition for the velocity (13) at the walls of the cavity, the classical half way bounce-back boundary condition is adopted. So, for example, consider the bottom wall for a boundary node x_b (see left figure of Fig. 2), the following bounce-back boundary condition is applied.

$$f_2(x_b, t + \Delta t) = f_4(x_e, t + \Delta t) = f_4^*(x_b, t),$$
$$f_5(x_b, t + \Delta t) = f_7(x_c, t + \Delta t) = f_7^*(x_b, t),$$
$$f_6(x_b, t + \Delta t) = f_8(x_d, t + \Delta t) = f_8^*(x_b, t).$$

For the thermal boundary condition, the Dirichlet boundary conditions given by Eqs. (15) and (14) on the left and right wall of the domain Ω are introduced. For a given constant temperature T, this can be archived using the following scheme in boundary node x_b on the right wall (see right figure of Fig. 2) :

$$g_3(x_b, t + \Delta t) = -g_1(x_e, t + \Delta t) + \frac{1}{36}(4 - \widetilde{\alpha} - 2\widetilde{\beta})T,$$
$$g_7(x_b, t + \Delta t) = -g_5(x_c, t + \Delta t) + \frac{1}{36}(4 + 2\widetilde{\alpha} + \widetilde{\beta})T,$$
$$g_6(x_b, t + \Delta t) = -g_8(x_d, t + \Delta t) + \frac{1}{36}(4 + 2\widetilde{\alpha} + \widetilde{\beta})T,$$

For the Neumann boundary condition on the top and bottom wall of the domain Ω given by Eq. (16), the classical "bounce back" scheme is adopted. Consider a boundary node x_b in the bottom wall (see right figure of Fig. 2), the following scheme is used.

$$g_2(x_b, t + \Delta t) = g_4(x_e, t + \Delta t) = g_4^*(x_b, t),$$
$$g_5(x_b, t + \Delta t) = g_7(x_c, t + \Delta t) = g_7^*(x_b, t),$$
$$g_6(x_b, t + \Delta t) = g_8(x_d, t + \Delta t) = g_8^*(x_b, t).$$

For more detail about how to reconstruct the above boundary condition for thermal problem see [7].

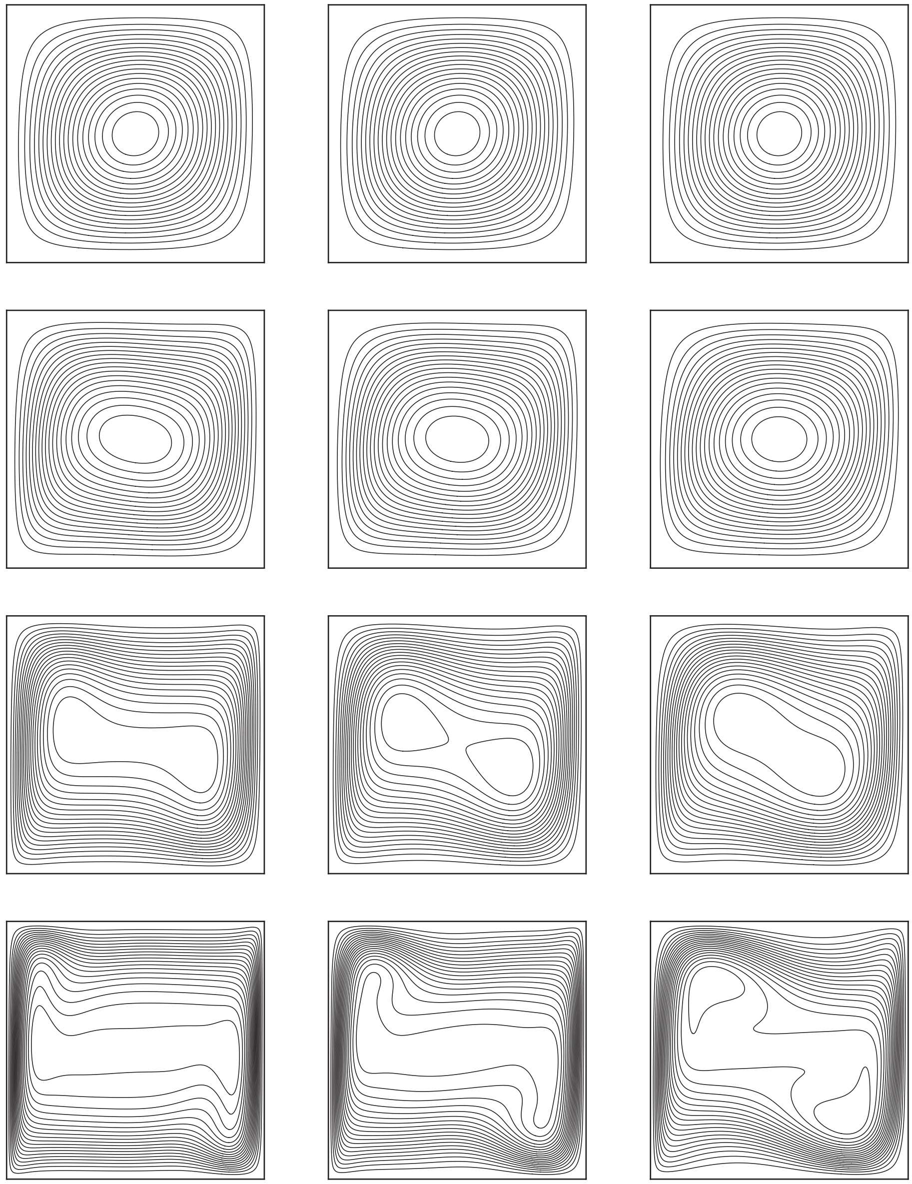

Fig. 6. Streamlines of flow fields (Ψ) for Pr=0.71. From top to bottom $Ra = 10^3$, 10^4, 10^5, and 10^6 respectively for mesh size 105^2, 155^2, 205^2 and 255^2. From left to right : (left) $\kappa_x = \kappa_y/2$, (center) isotropic case $\kappa_x = \kappa_y$,(right) $\kappa_x = 2\kappa_y$.

In the present parallel implementation, the single program multiple data (SPMD) environment is employed. Message-Passing-Interface (MPI) is adopted for the communication between the processors. The domain decomposition is done on direction of the computational domain, where the ghost cells are adopted along the inter-processor boundary.

3. Numerical results and discussion

3.1. Isotropic case

Let consider the isotropic thermal case, *i. e.* the x- thermal diffusivity κ_x is equal to $y-$ thermal diffusivity κ_y equal to a given thermal diffusivity κ. In this case we fix $\sigma_3 = \sigma_5$ to have $\kappa_x = \kappa_y$, described by Eq. (11), equal to the given thermal diffusivity κ. For the present natural convection within the square cavity as shown in Fig. 1, the major control parameter is the Rayleigh number $Ra = \beta \mathbf{g} \Delta T H^3 Pr/\nu^2$ associated with the heat transfer within the fluid, where H is the height or width of the cavity.

The Nusselt number is also an important dimensionless parameter in describing the convective heat transport. Its average in the whole flow domain is defined as,

$$\overline{Nu} = \frac{1}{\kappa \triangle T} \int_0^H q_x(x,y) dy \tag{17}$$

where $q_x(x,y) = uT(x,y) - \kappa\ \partial T(x,y)/\partial x$ is the local heat flux in the horizontal direction.

To compare with previous results, the main quantities to compute are : u_{max}, y, v_{max}, x and $\overline{Nu}$. Where u_{max} and its location y, the maximum vertical velocity on the horizontal mid-plane of the cavity, v_{max} and its location x, the maximum horizontal velocity on the vertical mid-plane of the cavity and the average Nusselt number $\overline{Nu}$.

We compute, for some cases, the maximum stream function ψ_{max} on the whole domain. Where the stream function is determined from:

$$\nabla.(\nabla \times \psi) = \frac{\partial v}{\partial x} - \frac{\partial u}{\partial y}.$$

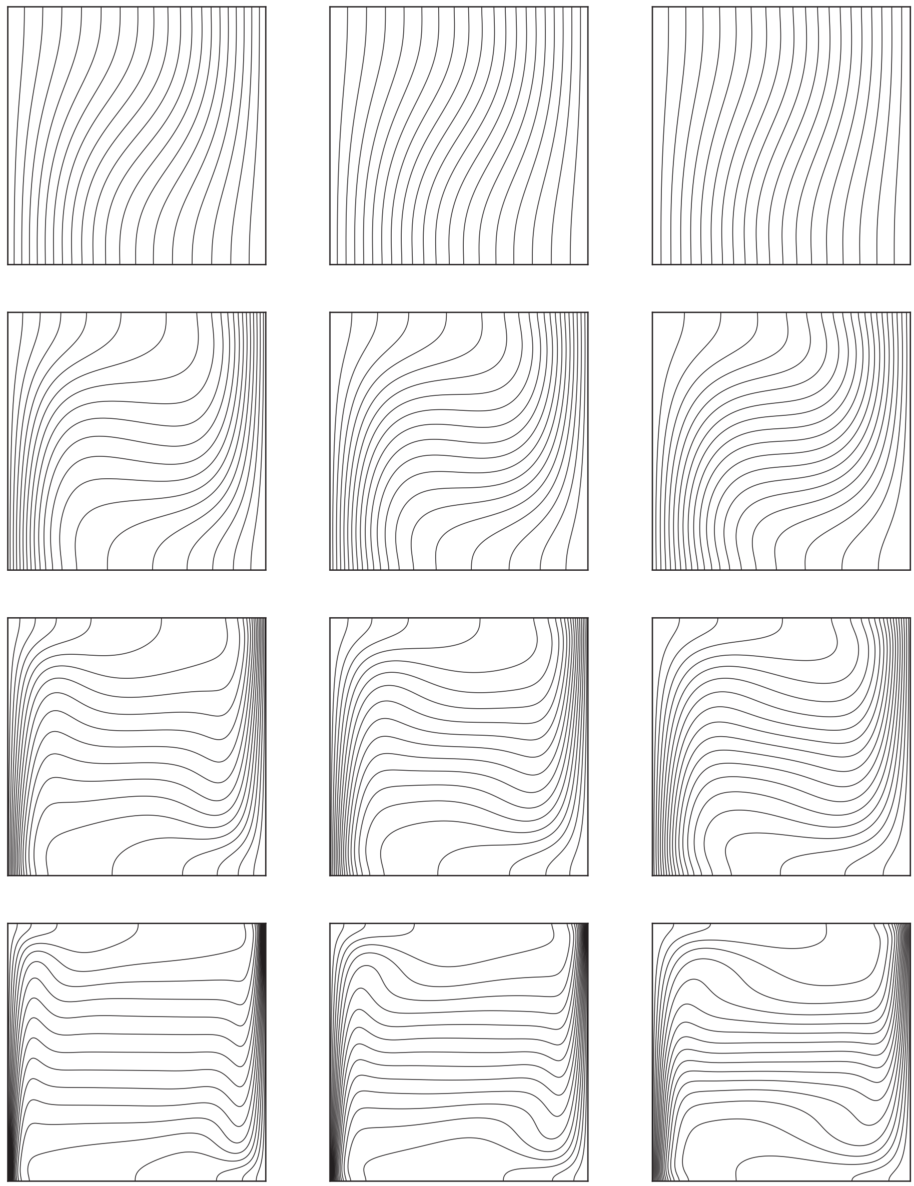

Fig. 7. Isotherms of flow fields (T) for Pr=0.71. From top to bottom $Ra = 10^3$, 10^4, 10^5, and 10^6 respectively for mesh size 105^2, 155^2, 205^2 and 255^2. From left to right : (left) $\kappa_x = \kappa_y/2$, (center) isotropic case $\kappa_x = \kappa_y$,(right) $\kappa_x = 2\kappa_y$.

Note here that for the computation of $\overline{Nu}$ described by Eq. (17), the temperature gradient $\frac{\partial T}{\partial x}$ is need. To calculate this gradient we do not do any additional interpolation method. In fact this quantity can be evaluated by using Taylor expansion [8] up to second-order of the non-conserved moment $\widetilde{m}_1$:

$$\widetilde{m}_1 = -\lambda^2 \Delta t \frac{1}{\sigma_\kappa}\left[\frac{4+\widetilde{\alpha}}{6}\frac{\partial T}{\partial x}\right] + O(\Delta t^2).$$

All the velocities are normalized using the diffusion velocity κ/H. The temperature are dimensionless, locations x and y are normalized using H.

3.2. Stability and admissible grid

Let define the Mach number as follows:

$$Ma = \frac{U}{C_s}, \tag{18}$$

where the quantity $U = \sqrt{\alpha g \Delta T H} = \sqrt{\frac{Ra}{Pr}}\frac{\nu}{H}$ is the characteristic velocity in thermal convective flows. So, to keep stability of the LBM scheme related dynamic field, the Mach number should be smaller than critical value $\frac{3}{10}$ (see [38] for more details). As in numerical simulation the parameters are fixed as $Pr = 0.71$ and $\nu = 0.01$, Eq. (18) gives a constrain on mesh size H. In fact, the mesh size must verify

$$\frac{10}{3}\frac{\nu}{C_s}\sqrt{\frac{Ra}{Pr}} < H. \tag{19}$$

Example for $Ra = 10^7$ and $Ra = 10^8$ the mesh size must satisfy $H > 216$ and $H > 685$, respectively.

3.3. Grid dependence

We begin by the study of the grid dependence and the accuracy of the scheme. In fact, Table 1 gives the results for the simulation for Rayleigh number $Ra = 10^6$ by using some different mesh sizes. We note that the calculated values approach the values given by the benchmark of de Vahl Davis [4] and the benchmark of Le Quéré [25]. In other hand table shows also second order accuracy for every measured quantities. Where the accuracy is calculated by least squares method using relative error between the solution obtained by mesh size N^2 and the reference one obtained by fine mesh ($N^2_{ref} = 1001^2$).

We have also see the grid dependance in the case of $Ra = 10^8$ for the following mesh size : 495 × 495, 987 × 987 and 2016 × 2016. The Table 2 shows that the quantities calculated quickly approach the values given by the benchmark of the Le Quéré [25]. We note here that the first grid size do not resolve the stability condition Eq. (19). But this size still gives a good solution.

3.4. Isotropic test case

Many papers study the square heated cavity, for the following 4 values of the Ra numbers : $Ra = 10^3, 10^4, 10^5$ and 10^6. So we compare our results to the following results: de Vahl Davis [4] benchmark solution where second order finite differences scheme and a Richardson extrapolation scheme are used, Mayne et al. [31] using h-adaptive finite element method, Kuznik et al. [21] and Liu et al. [28] using TLBM based on the BGK and Mezrhab et al. [33] and Wang et al. [38] using TLBM based on MRT D2Q9 for flow and MRT D2Q5 for temperature.

Table 3 shows the numerical results where the domain is covered by a lattice sizes of 105 × 105, 155 × 155, 205 × 205 and 255 × 255, respectively for $Ra = 10^3, 10^4, 10^5$ and 10^6 compared to the results obtained by the methods listed above. The simulated results are contrasted with the benchmark solutions of De Vahl Davis [4] and the agreements are satisfactory. It is also noted that differences of the predicted velocities and average Nusselt number are less than 0.1%. The middle column of Figs. 3–7 show the solution predicted by the present double D2Q9 MRT LBE method for Rayleigh numbers $Ra = 10^3$, for $Ra = 10^4$, $Ra = 10^5$ and $Ra = 10^6$ for isotropic case.

3.5. Anisotropic test case

In this section the effect of the anisotropy is performed. Let κ_x the x thermal diffusivity and κ_y the y thermal diffusivity. So we define the x Rayleigh number $Ra_x = \beta \mathbf{g} \Delta T H^3 \kappa_x / \nu$ associated with the x thermal diffusivity and $Ra_y = \beta \mathbf{g} \Delta T H^3 \kappa_y / \nu$ associated with the y thermal diffusivity. The choice of the anisotropy will be for different Rayleigh numbers fixed $Ra_y = 10^3, \ldots, 10^6$ as follows:

- x thermal diffusivity given by $\kappa_x = \dfrac{\kappa_y}{2}$.
- x thermal diffusivity given by $\kappa_x = 2\ \kappa_y$.

The average of Nusselt number in the whole flow domain is defined now as,

$$\overline{Nu} = \frac{1}{\kappa_x \Delta T} \int_0^H q_x(x, y) dy \tag{20}$$

where $q_x(x, y) = uT(x, y) - \kappa_x\ \partial T(x, y)/\partial x$ is the local heat flux in the horizontal direction.

To compare with isotropic results, the same main quantities to compute are : u_{max}, y, v_{max}, x and $\overline{Nu}$. We remark that all the velocities are normalized using the y diffusion velocity κ_y/H.

First we study the convergence and the accuracy of the scheme for anisotropic case. In fact, Tables 4 and 5 give the results for the simulation in case of Rayleigh number $Ra_y = 10^6$, for $\kappa_x = \frac{\kappa_y}{2}$ and $\kappa_x = 2\kappa_y$, respectively, by using some different mesh sizes. Tables 4 and 5 show also second order accuracy for every measured quantities. Here the accuracy is calculated by least squares method using relative error between the solution obtained by mesh size N^2 and the reference one obtained by fine mesh ($N^2_{ref} = 1001^2$).

Table 6 shows the numerical results for three different cases: $\kappa_x = \frac{\kappa_y}{2}$, $\kappa_x = \kappa_y$ (isotropic case) and $\kappa_x = 2\kappa_y$. The domain is covered by a lattice sizes of 105 × 105, 155 × 155, 205 × 205 and 255 × 255, respectively for $Ra_y = 10^3, 10^4, 10^5$ and 10^6. We note here that the u_{max} and v_{max} increase when the κ_x increase. This is due to the fact of the imposed hot wall (at $x = 0$) and cold wall (at $x = 1$) is in x direction.

Figs. 3–7 show the solution predicted by the present double D2Q9 MRT LBE method for Rayleigh numbers $Ra_y = 10^3, 10^4, 10^5$ and 10^6 for anisotropic case. We refind here that the effect of x thermal diffusivity κ_x is more important than y thermal diffusivity κ_y. In fact when $\kappa_x = 2\kappa_y$ the velocity of the fluid is bigger.

4. Conclusion

In this paper, a multi-relaxation time thermal lattice Boltzmann scheme has been applied to compute natural convection flow within differential heated square cavity. For Rayleigh number under 10^6 the present results compare favorably with previous benchmark solutions. Then anisotropic thermal diffusion is investigated ($\kappa_x = \frac{\kappa_y}{2}$ and $\kappa_x = 2\kappa_y$). The solution is compared to the isotropic case. We note the ability of double D2Q9 population to resolve anisotropic problem. Finally we remark when the x thermal diffusivity κ_x increase the velocity of the fluid increase and the convergence of the scheme to the steady state is faster.

Acknowledgments

The authors thank Pierre Lallemand (Beijing Computational Science Research Center, Beijing, China) for helpful discussion during the elaboration of this work. Many thanks also to the support by the Taiwan National Science Council (Grant 94-2212-E-007-059) and the computational facilities provided by the Taiwan National Center for High-Performance Computing.

References

[1] Alexander FJ, Chen S, Sterling JD. Lattice Boltzmann thermodynamics. Phys Rev E 1993;47:2249.
[2] Bespalko D, Pollard A, Uddin M. Analysis of the pressure fluctuations from an LBM simulation of turbulent channel flow. Comput Fluids 2012;54:143.
[3] Contrino D, Lallemand P, Asinaria P, Luo L. Lattice-Boltzmann simulations of the thermally driven 2D square cavity at high Rayleigh numbers. J Comput Phys 2014;275:257–72.
[4] De Vahl Davis G. Natural convection of air in a square cavity: a bench mark numerical solution. Int J Numer Methods Fluids 1983;3:249.
[5] Dubois F. Equivalent partial differential equations of a lattice Boltzmann scheme. Comput Math Appl 2008;55:1141–9.
[6] Dubois F, Lallemand P. Towards higher order lattice Boltzmann schemes. J Sta Mech: Theory Exp 2009;2009:06006.
[7] Dubois F, Lallemand P, Tekitek MM. Using lattice Boltzmann scheme for anisotropic diffusion. Finite Volumes for Complex Applications V, 795. London: ISTE, Wiley; 2008.
[8] Dubois F, Lallemand P, Tekitek MM. On a superconvergent lattice Boltzmann boundary scheme. Comput Math Appl 2010;59:2141.
[9] Dubois F, Lallemand P, Tekitek MM. Taylor Expansion Method for Linear Lattice Boltzmann Schemes with an External Force: Application to Boundary Conditions. Lecture Notes in Computational Science and Engineering, 99. European Workshop HONOM 2013, Bordeaux, France, March 18-22, Springer; 2014. p. 89–107.
[10] Dixit HN, Babu V. Simulation of high Rayleigh number natural convection in a square cavity using the lattice Boltzmann method. Int J Heat Mass Transf 2006;49:727.
[11] Flückiger R, Freunberger SA, Kramer D, Wokaun A, Scherer GG, Büchi FN. Anisotropic, effective diffusivity of porous gas diffusion layer materials for PEFC. Electrochim Acta 2008;54:551.
[12] Frisch U, d'Humières D, Hasslacher B, Lallemand P, Pomeau Y, Rivet J-P. Lattice gas hydrodynamics in two and three dimensions. Complex Syst 1987;1:649–707.
[13] Ginzburg I. Equilibrium-type and link-type lattice Boltzmann models for generic advection and anisotropic-dispersion equation. Adv Water Resour 2005;28:1171–95.
[14] Ginzburg I, Adler P. Boundary flow condition analysis for the three-dimensional lattice Boltzmann model. J Phys II 1994;4:191–214.
[15] Ginzburg I, d'Humières D. Lattice Boltzmann and analytical modeling of flow processes in anisotropic and heterogeneous stratified aquifers. Adv Water Resour 2007;30:2202–34.
[16] Guo Z, Shi B, Zheng C. A coupled lattice BGK model for the Boussinesq equations. Int J Numer Methods Fluids 2002;39:325.
[17] Guo ZL, Zheng CG, Shi BC. Discrete lattice effects on the forcing term in the lattice Boltzmann method. Phys Rev E 2002;65:1. Article Number: 046308.

[18] Guo Z, Zheng C, Shi B. Thermal lattice Boltzmann equation for low Mach number flows: decoupling model. Phys Rev E 2007;75:15.

[19] He X, Chen S, Doolen GD. A novel thermal model for the lattice Boltzmann method in incompressible limit. J Comput Phys 1998;146:282.

[20] He XY, Luo LS. Lattice Boltzmann model for the incompressible Navier–Stokes equation. J Stat Phys 1997;88:927.

[21] Kuznik F, Vareilles J, Rusaouen G, G Krauss G. A double-population lattice Boltzmann method with non-uniform mesh for the simulation of natural convection in a square cavity. Int J Heat Fluid Flow 2007;28:862.

[22] Lallemand P. Improve LBE Model, Summer School on the Lattice Boltzmann Method. Beijing Computational Science Research Center; 2012.

[23] Lallemand P, Luo L. Theory of the lattice Boltzmann method: dispersion, dissipation, isotropy, Galilean invariance, and stability. Phys Rev E 2000;61:6546–62.

[24] Lallemand P, Luo L-S. Hybrid finite-difference thermal lattice Boltzmann equation. Int J Mod Phys B 2003;17:41.

[25] Quéré PL. Accurate solutions to the square differentially heated cavity at high Rayleigh number. Comput Fluids 1991;20:19.

[26] Lin L-S, Chen Y-C, Lin C-A. Multi relaxation time lattice Boltzmann simulations of deep lid driven cavity flows at different aspect ratios. Comput Fluids 2011;45:233.

[27] Lin K-H, Liao C-C, Lien S-Y, Lin C-A. Thermal lattice Boltzmann simulations of natural convection with complex geometry. Comput Fluids 2012;69:35.

[28] Liu CH, Lin KH, Mai HC, Lin CA. Thermal boundary conditions for thermal lattice Boltzmann simulations. Comput Math Appl 2010;59:2178.

[29] Mai H-C, Lin K-H, Yang C-H, Lin C-A. A thermal lattice Boltzmann model for flows with viscous heat dissipation. Comput Model Eng Sci 2010;61:45.

[30] Massaioli F, Benzi R, Succi S. Exponential tails in two-dimensional Rayleigh–Benard convection. Europhys Lett 1993;21:305.

[31] Mayne DA, Usmani A, Crapper M. h-Adaptive finite element solution of unsteady thermally driven cavity problem. Int J Numer Methods Heat Fluid Flow 2000;10:598.

[32] McNamara G, Garcia AL, Alder BJ. Stabilization of thermal lattice Boltzmann models. J Stat Phys 1995;81:395.

[33] Mezrhab A, Moussaoui MA, Jami M, Naji H, Bouzidi M. Double MRT thermal lattice Boltzmann method for simulation convective flows. Phys Lett A 2010;374:3499.

[34] Pasaogullari U, Mukherjee PP, Wang C-Y, Chen KS. Anisotropic heat and water transport in a PEFC cathode gas diffusion layer. J Electrochem Soc 2007;154:823.

[35] Peng Y, Shu C, Chew YT. Simplified thermal lattice Boltzmann model for incompressible thermal flows. Phys Rev E 2003;68:026701.

[36] Shi Y, Zhao TS, Guo ZL. Thermal lattice Bhatnagar–Gross–Krook model for flows with viscous heat dissipation in the incompressible limit. Phys Rev E 2004;70:066310.

[37] Shih C-H, Wu C-L, Chang L-C, Lin C-A. Lattice Boltzmann simulations of incompressible liquid-gas systems on partial wetting surfaces. Philos Trans R Soc A – Math Phys Eng Sci 2011;369:2510.

[38] Wang J, Wang DH, Lallemand P, Luo L-S. Lattice Boltzmann simulations of thermal convective flows in two dimensions. Comput Math Appl 2013;65:262–86.

[39] Yu DZ, Mei RW, Luo L-S, Shyy W. Viscous flow computations with the method of lattice Boltzmann equation. Prog Aeosp Sci 2003;39:329.